Optics Letters

Improved nondegenerate multiphoton microscopy and axial registration with a reflective objective

Ahmed M. Hassan, Shaun Engelmann, and Andrew K. Dunn*

Department of Biomedical Engineering, The University of Texas at Austin, 107 W. Dean Keeton C0800, Austin, Texas 78712, USA
*Corresponding author: adunn@utexas.edu

Conventional, degenerate multiphoton microscopy (D-MPM) requires the use of a high-numerical-aperture (NA) objective. Nondegenerate MPM (ND-MPM) imposes the additional demand for precise spatiotemporal overlap of two distinct excitation sources. We demonstrate that the axial focal shift introduced by refractive objective chromatic aberration hinders the spatial requirement of ND-MPM, whereas the use of a reflective objective overcomes this challenge and allows for improved ND excitation efficiency in spite of a lower NA. Moreover, we demonstrate that reflective objective focusing eliminates the axial misregistration of volumetric stacks in traditional D-MPM experiments when multiple excitation wavelengths are used. © 2019 Optical Society of America

https://doi.org/10.1364/OL.44.005017

Conventional, or degenerate, multiphoton microscopy (D-MPM) relies on the absorption of two or more spatiotemporally overlapped photons of identical energies [1]. Nondegenerate multiphoton microscopy (ND-MPM) combines synchronized pulses from two lasers of different wavelengths (λ_1 and λ_2) to excite a fluorophore transition [2,3]. Provided the two pulses arrive to the same location at the same time, the energies of the photons add at an effective excitation wavelength given by $\lambda_3 = 2(\lambda_1^{-1} + \lambda_2^{-1})^{-1}$ [4]. ND-MPM has several unique advantages, including simultaneous multicolor imaging capabilities [4,5], improved signal-to-background ratio [6], and the ability to excite fluorophores with substrate-incompatible absorptions at the virtual λ_3 wavelength. Notably, the total excitation of the combined beams is given by the cross-correlation term $(I_1 + I_2)^2 = I_1^2 + I_2^2 + 2I_1 I_2$, where I_1^2 is the excitation profile (i.e., point spread function, or PSF) at λ_1, I_2^2 dictates the PSF at λ_2, and $2I_1 I_2$ dictates the PSF at λ_3 [4]. The ability to target a fluorophore at λ_3 with ND-MPM, yet probabilistically stimulate fluorescent events at all three excitation pathways, has been shown to achieve a significant increase in excitation efficiency relative to D-MPM [7].

Traditional multiphoton objectives are composed of a series of refractive lenses that compensate for one another's aberrations. High-quality objectives are commonly corrected to improve image quality by minimization of spherical aberration, coma, astigmatism, and distortion. Unfortunately, chromatic aberration is unavoidable with refractive objectives, meaning that distinct wavelengths are focused at different optical z-planes. Achromat objectives tailored to minimize this undesired effect can only provide chromatic correction over a limited spectral range (e.g., the visible regime) and are ill-suited for ND-MPM, which can demand the spatial overlap of wavelength combinations spanning the visible, near-infrared (NIR), or IR spectrum [7,8]. While electrically tunable lenses and remote focusing enable variable axial focus [9], modulation by these elements is common to both ND scan paths and cannot be used to achieve mutual overlap. In principle, a simple relay can be used to apply defocus to a single excitation beam and compensate for chromatic focal offset. In practice, however, it is challenging to avoid vignetting an acollimated beam through an optical system, and this defocus directly broadens the beam's PSF, which thereby reduces multiphoton excitation efficiency and, more importantly, spatial resolution.

An effective and simple solution to circumvent chromatic aberration and overlap the focused profiles of independent laser sources for ND-MPM is to employ a reflective objective. Typical reflective objectives use a pair of curved mirrors to achieve near- or diffraction-limited focusing and image magnification [10]. Reflective objectives provide achromatic focusing capabilities, eliminate the adverse effects of dispersion, and can successfully coalign independent laser sources at discrete wavelengths in the sample plane [11,12]. In spite these advantages, they have yet to be adopted for ND-MPM, perhaps due to obscuration, polarization maintaining issues, and their relatively low numerical apertures (NA). Obscuration refers to mechanical light attenuation from mirror design, where a significant portion of light entering the objective fails to reflect to a secondary mirror, and an additional fraction is obstructed by thin suspensions used to mount the primary mirror. Encouragingly, simulation has shown that back-reflections may be minimized by the adoption of annular-shaped beams in favor of Gaussian profiles [13]. Moreover, reflective objectives' transmission properties (>99% from 450 nm to 20 μm) vastly outperform traditional refractive objectives with NIR coatings, including optimized multiphoton objectives (~70% from 1100 to 1400 nm) [14]. Recalling that ND-MPM enhances excitation efficiency relative to D-MPM, allowing one to trade excitation efficiency for laser power [15], taken with

reflective objectives' improved transmission properties, obscuration becomes a minor drawback. However, the low NA of reflective objectives still poses a major concern. Here we demonstrate that the improved ND axial overlap of reflective objectives increases ND excitation efficiency relative to even higher NA refractive objectives.

To evaluate the axial focal shift severity of refractive versus reflective objectives, a tunable nonlinear optical parametric amplifier (Spirit-NOPA-VISIR, Spectra-Physics) was focused onto a photodiode (G1117, Hamamatsu) using a 10× refractive objective (MRL00102, 0.25 NA, Nikon, air), a 20× refractive objective (XLUMPLFLN, 1.0 NA, Olympus, water immersion), and a 40× reflective objective (LMM-40X-P01, 0.5 NA, Thorlabs, air). The 10× is a plan achromat objective whose low NA increases the axial PSFs of the focused beams, which can be advantageous for two-color overlap. On the other hand, the 20× objective is specialized for MPM [16], and offers semi-apochromat performance from the visible to IR range at a high NA. Thus, it was determined that each refractive objective could serve as a distinct use case comparison to the reflective objective. The photosensor material, GaAsP, was selected due to its broad multiphoton excitation spectrum, allowing focal shift to be evaluated over a wide wavelength tuning range. Fluorescence intensity of the GaAsP film was recorded as a function of axial position, which was dynamically adjusted using a motorized labjack platform at excitation wavelengths ranging from 1150 to 1550 nm. The peaks of interpolated fits to the resulting fluorescence intensity curves were used to indicate axial focus at each wavelength [Fig. 1(a)]. Axial focal shift is most severe with the 10× objective (±80 μm, $\Delta\lambda = 400$ nm, $PSF_{axial} \sim 25.99$ μm), followed by the 20× objective (±10 μm, $\Delta\lambda = 400$ nm, $PSF_{axial} \sim 2.62$ μm), whereas the reflective objective exhibits less than ~2 μm of axial focal shift ($\Delta\lambda = 400$ nm, $PSF_{axial} \sim 11.39$ μm). Since

the reflective objective is expected to be free of chromatic aberration, it is possible that this modest shift is owed to refractive effects in the scan and tube lens relay and wavelength-dependent Gaussian beam divergence.

When these results are placed into context with the modeled axial PSF length of each objective [17], it is evident that efficient ND-MPM is precluded by either refractive objective [Fig. 1(b)]. Maximally efficient ND-MPM demands minimal focal shift and a smaller PSF. However, in the presence of substantial focal shift, a larger PSF can compensate to improve ND overlap and hence relative nondegenerate excitation, at the tradeoff of reduced overall MPM excitation efficiency. However, the severe focal shift of the refractive 10× objective overwhelms even its relatively large PSF, and the small PSF of the refractive 20× objective prevents effective ND overlap in spite of a moderate focal shift. It is observed that the axial dimension of the reflective objective's PSF exceeds the expected axial shift across the 400 nm spectral range, suggesting that its ND-MPM efficiency would be superior to the refractive objectives.

A byproduct of axial focal shift is that imaged structures must be refocused as excitation wavelength is tuned. To confirm this effect and ensure that the previously observed axial focal shift was not a possible artifact of stratified layers in the GaAsP photosensor exhibiting wavelength-dependent absorption cross sections, a monolayer of quantum dots (QD605, Thermofisher Scientific) was prepared and imaged at 50 nm wavelength increments ranging from 1150 to 1500 nm. Quantum dots were chosen due to their brightness, photostability, and broad absorption spectrum. For each objective, a reference image was chosen from a focused slice of the $\lambda_{ex} = 1150$ nm z-stack, and its structural similarity index measure (SSIM) was calculated relative to all other images (Fig. 2) by computing correlation as a product of luminance, contrast, and structural similarity [18]. A larger SSIM score for an image indicates a higher degree of similarity to the reference image.

For the 10× refractive objective, roughly ~125 μm of axial focal shift is evidenced by the SSIM scores between 1150 and 1500 nm, with the focal shift being linear and consistently offset at each wavelength increment [Fig. 2(a)]. Calculated SSIM scores of images collected by the 20x objective reveal a similar, but muted, effect with approximately ~18 μm of axial focal shift across the same spectral range [Fig. 2(b)]. Interestingly, the direction of axial shifts in the SSIM heat maps are reversed for the two refractive objectives, indicating the lower and higher magnification objectives introduce dispersion in opposite directions. Finally, the 40× objective reveals a very slight focal shift. The nonlinearity of the shift suggests that it cannot be solely explained by wavelength-dependent Gaussian beam divergence, which itself is linear. In addition, the bright bands, which indicate focused regions with a high degree of image similarity, narrow as excitation wavelength increases with the 40× data. This is an unexpected result with respect to axial PSF length, which increases at longer excitation wavelengths. This observation highlights a critical point of clarification—the widths of these bands is not a direct measurement of the axial PSF length. Rather, the SSIM magnitude at each plane, and thus the apparent widths of each band, is the complement of many wavelength-dependent effects including spectral bandwidth, absorption cross section, scattering length, and n-photon power dependence, in addition, but not limited to axial PSF length.
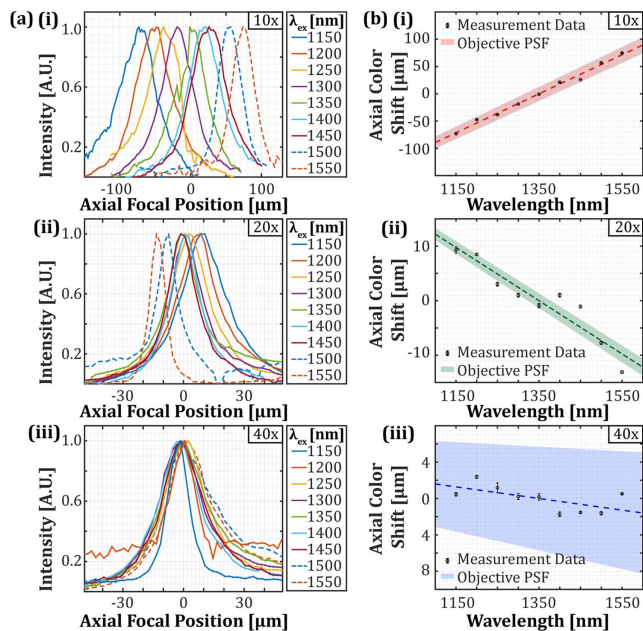

Fig. 1. (a) Fluorescence intensity curves versus axial focal position characterizes axial focal shift for refractive (i, 10×; ii, 20×) and reflective (iii, 40×) objectives. (b) Axial focal shift values versus excitation wavelength plotted against modeled axial point spread function full width at half-maximum (shaded regions).
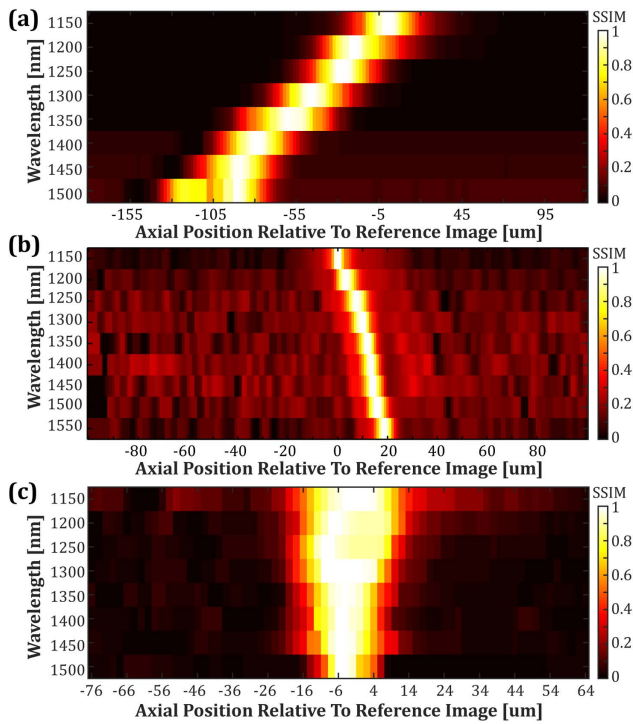
Fig. 2. Structural-similarity index measurements (SSIM) of individual slices from z-stacks recorded at discrete excitation wavelengths with (a) a 10× refractive objective, (b) a 20× refractive objective, and (c) a 40× reflective objective. For each objective, the SSIM scores were recorded relative to a well-focused reference image from the $\lambda_{ex} = 1150$ nm stacks.

Fig. 3. Transverse max intensity projections of a cellular monolayer recorded with (a) a 10× refractive objective, (b) a 20× refractive objective, and (c) a 40× reflective objective. (d) Mean image intensity versus depth for the 10× (dashed lines), 20× (finely dashed lines), and 40× (solid lines) objectives. The green channel contains Alexa Fluor 488 signal, $\lambda_{ex} = 790$ nm, and the red channel denotes Alexa Fluor 594 signal and second-harmonic generation, $\lambda_{ex} = 1300$ nm. Scale bar = 75 μm.

Modern-day biological microscopy studies are often highlighted by the variety and number of structures that are targeted, labeled, and imaged. Such multiplexed imaging experiments typically feature two distinct approaches: multispectral and multicolor. Emission-based multispectral imaging uses a single excitation wavelength to simultaneously excite unique fluorescent targets separated by the appropriate emission filter sets. In excitation-based multicolor imaging, distinct populations of fluorophores with overlapping emission spectra can instead be resolved separately by targeting discrete populations with highly specific excitation wavelengths. Both are widely used techniques, along with other hybrid approaches. However, 3D imaging experiments that employ the latter excitation-based multiplexed imaging technique unveil the risk of an axial misregistration of the separate excitation channels when refractive objectives are used. To demonstrate this, matching regions of a fixed human brain microvascular endothelial cell monolayer sample with Alexa Fluor 488-labeled junction adhesion molecule (Alex Fluor 488-Ab-JAM) and Alexa Fluor 594-labeled occludin (Alexa Fluor 594-Ab-Occludin) were imaged with both refractive and reflective objectives (Fig. 3). Alexa Fluor 488, $\lambda_{ex} = 790$ nm, was detected through a 510/84 bandpass filter (FF01-510-25, Semrock), and Alexa Fluor 594, $\lambda_{ex} = 1300$ nm, was detected through a 610/75 bandpass filter (HQ610/75M, Chroma Technology Corp). Due to the specific combination of excitation wavelength and emission filter used to target Alexa Fluor 594, second-harmonic generation (SHG) of collagen fibers could be seen along with the occludin. 3D stacks of the cellular samples were recorded, and the mean intensity of
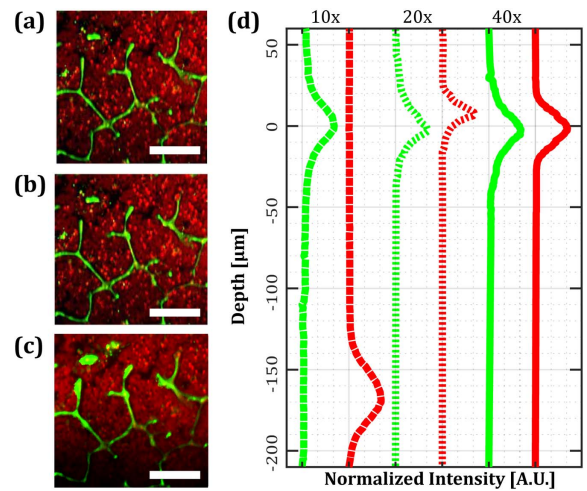
each 2D image was calculated as function of depth to delineate the axial misregistration of the separate channels. Maximum intensity z-projections reveal there is no lateral shift between the separate excitation stacks and that identical regions were imaged across the 10, 20, and 40× objectives [Figs. 3(a)–3(c)]. The intensity versus depth curves denote that axial misregistration with the 10× objective is significantly pronounced such that there is no evidence of cellular colocalization between the JAM and occludin structures, each occupying regions that falsely appear to be ~175 μm apart, despite the specimen being a monolayer [Fig. 3(d)]. The misregistration caused by the 20× objective is much more subtle; however, mean image intensity versus depth reveals that the Alexa Fluor 594 signal is shifted ~10 μm relative to the Alexa Fluor 488 signal, whereas the multichannel data recorded with the reflective objective presents perfect overlap. The higher magnification refractive objective's shift is less acute than the GaAsP and QD605 results, which were evaluated at longer excitation wavelengths, suggesting that its achromat performance is improved at the shorter end of the NIR spectrum. Lastly, the 20× objective's axial shift direction is opposite to the 10×, an effect that remains consistent with prior results.

ND-MPM efficiency is directly determined by the precise overlap of the two synchronized laser sources' PSFs in the focal plane. Results thus far suggest that the refractive objectives' axial focal shift hinders accurate ND overlap relative to the reflective objective. To quantify the impact of this effect on ND-MPM efficiency, a GaAsP photosensor was simultaneously excited with the shorter and longer wavelengths of the signal and idler outputs of a NOPA laser, respectively (Fig. 4). Idler excitation wavelength ranged from $\lambda_1 = 1150$ to 1350 nm, and signal excitation wavelength was maintained at $\lambda_2 = (515\,\text{nm}^{-1} - \lambda_1^{-1})^{-1}$ to achieve a constant virtual excitation wavelength $\lambda_3 = 1030$ nm. To evaluate ND-MPM excitation efficiency at various combinations of λ_1 and λ_2, the signal beam was aligned through an optical delay line, allowing the beam to
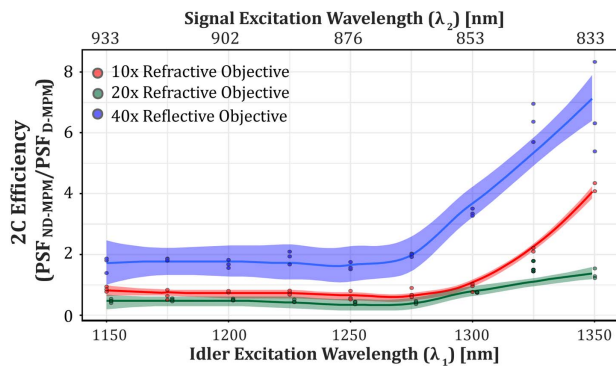
Fig. 4. Nondegenerate excitation efficiency comparison of the refractive and reflective objectives; scatter points denote raw data, solid lines indicate regression fits, and shaded regions demarcate corresponding 95% confidence intervals.

be temporally swept through the idler without affecting spatial overlap. The peak of the fluorescence emission as a function of delay line position is the result of precise temporal overlap of the two focused excitation pathways, the total excitation of which is given by $I_1^2 + I_2^2 + 2I_1I_2$. As the optical delay line deviates from this position, the resulting fluorescence intensity is solely a consequence of the individual D-MPM events at λ_1 and λ_2, $\text{PSF}_{\text{D-MPM}} = I_1^2 + I_2^2$, in the absence of the ND-MPM event at λ_3, given by $\text{PSF}_{\text{ND-MPM}} = 2I_1I_2$. Thus, ND excitation efficiency can be calculated for each objective by subtracting fluorescent intensity values at a 500 fs optical delay from intensity values at precise temporal overlap to isolate the ND-MPM excitation profile, then normalizing it relative to the delayed D-MPM intensity. Since nondegenerate emission intensity is proportional to the power of each beam [7], absorbed power in the GaAsP photosensor was measured as a voltage signal and set constant for all excitation wavelengths and each objective.

For all three objectives, ND efficiency remains consistently small between 1150 and 1250 nm, before a substantial increase at 1300 nm. This suggests that the GaAsP cross section at 1030 nm is similar to the 1150 to 1250 nm or 876 to 933 nm cross sections, but quite high compared to the >1250 and <876 nm cross sections. More importantly, we observe that the ND efficiency of the 40× objective is larger than the 10× and 20× objectives' ND efficiency at all excitation wavelength combinations, demonstrating that the improved axial overlap of the reflective objective confers enhanced properties for ND-MPM. Yet another factor that may contribute to the refractive objectives' deficient excitation efficiency is pulse broadening caused by group velocity dispersion, which was not precompensated for in this work. Notably, the outperformance of the reflective objective relative to the refractive objectives increases as $\Delta\lambda = \lambda_1 - \lambda_2$ widens. This suggests that an increase in the refractive objectives' axial focal shift severity with larger $\Delta\lambda$ further degrades refractive ND efficiency.

However, it remains surprising that the refractive objectives exhibit any nondegenerate excitation signal with respect to the results shown in Fig. 1, which strongly indicate that there is little overlap between the ND focal profiles. This may be explained by the broad spectral bandwidth of the short pulse excitation sources, which helps maintain spectral, and therefore axial, overlap. Furthermore, due to random scatter of the ND photons and the probabilistic nature of multiphoton excitation,

the likelihood of a nondegenerate excitation event remains non-zero even in cases of completely nonoverlapping PSFs. This is visibly evident in the SSIM results (Fig. 2), where similarity bands at different wavelengths exhibit a significant degree of overlap. This is further supported by the ND efficiency plot, which shows that the 10× objective slightly outperforms the 20× objective, possibly due to the 10× objective's enlarged PSF allowing for an expanded scattering radius. Of course, sophisticated ray tracing and modeling are needed to fully support this claim. Collectively, these experiments demonstrate that a 0.5 NA reflective objective can outperform a higher NA refractive objective for ND-MPM, despite the latter's precedence in conventional MPM. Moreover, direct comparison to a lower NA refractive objective demonstrates that reflective objectives' advantage for ND-MPM applications stems from their minimal axial focal shift, rather than an enlarged axial PSF, although both qualities help to improve two-color overlap. Continued development in reflective objective technology to increase their NA while maintaining achromatic capabilities will undoubtedly lead to further gains in this area.

REFERENCES

1. F. Helmchen and W. Denk, Nat. Methods **2**, 932 (2005).
2. D. Fu, T. Ye, T. E. Matthews, G. Yurtsever, and W. S. Warren, J. Biomed. Opt. **12**, 054004 (2007).
3. M.-H. Yang, M. Abashin, P. A. Saisan, P. Tian, C. G. L. Ferri, A. Devor, and Y. Fainman, Opt. Express **24**, 30173 (2016).
4. P. Mahou, M. Zimmerley, K. Loulier, K. S. Matho, G. Labroille, X. Morin, W. Supatto, J. Livet, D. Débarre, and E. Beaurepaire, Nat. Methods **9**, 815 (2012).
5. C. Stringari, L. Abdeladim, G. Malkinson, P. Mahou, X. Solinas, I. Lamarre, S. Brizion, J.-B. Galey, W. Supatto, R. Legouis, A.-M. Pena, and E. Beaurepaire, Sci. Rep. **7**, 3792 (2017).
6. D. Kobat, G. Zhu, and C. Xu, in Biomedical Optics (Optical Society of America, 2008), paper BMF6.
7. M.-H. Yang, M. Abashin, P. A. Saisan, A. Devor, and Y. Fainman, in Optics and the Brain (Optical Society of America, 2015), paper BrW3B.6.
8. S. Quentmeier, S. Denicke, and K.-H. Gericke, J. Fluoresc. **19**, 1037 (2009).
9. J. Jiang, D. Zhang, S. Walker, C. Gu, Y. Ke, W. H. Yung, and S. Chen, Opt. Express **23**, 24362 (2015).
10. H. Wang, X. Yang, Y. Liu, B. Jiang, and Q. Luo, Opt. Express **21**, 24210 (2013).
11. B. Amirsolaimani, B. Cromey, N. Peyghambarian, and K. Kieu, Opt. Express **25**, 23399 (2017).
12. V. Raghunathan, Y. Han, O. Korth, N.-H. Ge, and E. O. Potma, Opt. Lett. **36**, 3891 (2011).
13. M. M. Kabir, A. M. Choubal, and K. C. Toussaint, J. Microsc. **271**, 129 (2018).
14. D. R. Miller, "Extending the depth limit of multiphoton microscopy for in vivo brain imaging," Ph.D. dissertation (The University of Texas at Austin, 2016).
15. S. Sadegh, M.-H. Yang, C. G. Ferri, M. Thunemann, P. A. Saisan, E. A. Rodriguez, S. R. Adams, S. A. Vinogradov, Y. Fainman, and A. Devor, in Optics and the Brain (Optical Society of America, 2018), paper BF3C.2.
16. J. P. Zinter and M. J. Levene, Opt. Express **19**, 15348 (2011).
17. M. Leutenegger, R. Rao, R. A. Leitgeb, and T. Lasser, Opt. Express **14**, 11277 (2006).
18. Z. Wang, A. C. Bovik, H. R. Sheikh, and E. P. Simoncelli, IEEE Trans. Image Process. **13**, 600 (2004).